Unified modeling of turbulence effects on sound propagation

Sylvain Cheinet[a] and Loic Ehrhardt
Institut Franco-Allemand de Recherches de Saint-Louis (ISL), 5 Rue du Général Cassagnou, 68 300 Saint-Louis, France

Daniel Juvé and Philippe Blanc-Benon
Laboratoire de Mécanique des Fluides et d'Acoustique (LMFA), École Centrale de Lyon, 36, Avenue Guy de Collongue, 69134 Écully, France

(Received 26 October 2011; revised 16 July 2012; accepted 10 August 2012)

Many aspects of outdoor sound propagation depend on the scattering effects induced by atmospheric turbulence. Standard analytical and numerical assessments of these effects make an *a priori* distinction between the scattering effects at large versus small angles. The present study evaluates the ability of a numerical model in overcoming this distinction. The model solves a set of two coupled equations for the sound pressure and vector acoustic velocity, with the finite-difference time domain approach. It is first introduced and evaluated. The numerical predictions are compared to well-known analytical solutions in the case of two-dimensional plane wave propagation through turbulence. They are found to agree in the investigated scenarios. Hence, the finite-difference, time domain solution of the two coupled equations provides a unified, versatile numerical approach to investigating the effects of atmospheric turbulence on sound propagation. The comparison also provides original insights on the applicability and limitations of various methods used to investigate sound propagation through turbulence. © *2012 Acoustical Society of America*.
[http://dx.doi.org/10.1121/1.4748584]

PACS number(s): 43.28.Gq, 43.28.Js, 43.28.Lv [VEO] Pages: 2198–2209

I. INTRODUCTION

Atmospheric turbulence has a major impact on outdoor sound propagation. It causes the penetration of sound in shadow zones and in interference fringes (Wiener and Keast, 1959, Daigle, 1979). It may also distort the propagating signal (Havelock *et al.*, 1995, McLeod *et al.*, 2004). For the inverse problem configuration, these alterations to the propagating wave may be used to remotely sense the atmospheric turbulence properties (e.g., Wilson and Thomson, 1994; Vecherin *et al.*, 2006).

The experimental characterization of these effects raises major difficulties. The wave characteristics and the atmospheric fluctuations cannot be measured simultaneously along the propagation path. In addition to the effects of atmospheric turbulence, the other environmental effects must also be considered, such as those due to ground reflection and atmospheric stratification. Experiments must therefore be complemented by theoretical considerations, which provide an idealized but controlled and reproducible assessment of the physics at play.

Tatarski (1961) (hereafter, T61) gives an analytical investigation of wave propagation through turbulence. Its starting point is a Helmholtz-type propagation equation for a monochromatic wave. T61 distinguishes between two scenarios, with distinct physical assumptions and mathematical treatments. In the first scenario, the propagation is analyzed at large scattering angles and far from the scattering volume [Fig. 1(a)]. The second scenario considers the line-of-sight propagation [Fig. 1(b)].

Many studies have elaborated on the results of T61, e.g., Tatarski (1971). Analytical and numerical studies have examined the large scattering angle case in the presence of realistic atmospheric conditions (Goedecke and Auvermann, 1997; Ye, 1997; Wilson *et al.*, 1996). The line-of-sight investigations have been extended (Dashen, 1979), with parabolic equation (PE) models (Martin and Flatté, 1988; Gilbert *et al.*, 1990) or in presence of ground reflection (Ostashev *et al.*, 2001). Reference textbooks on the topic may be found, e.g., Wheelon (2003). In terms of applications, the sound detection and ranging technology remotely senses the atmospheric turbulence on the basis of the large-angle scattering solutions of T61 (e.g., Kallistratova, 1997; Coulter, 1997).

Still, the separate treatment with the scattering angle largely holds in the literature, e.g., Cotté and Blanc-Benon (2007). The theory based on the diagram technique overcomes the separation (Ostashev, 1997), but its applicability in realistic propagation cases remains to be established. This persistent separation challenges a comprehensive, unified assessment of the scattering effects. It hampers a direct comparison of the predictions with outdoor propagation experiments (Daigle *et al.*, 1986). Besides, the assumptions required to obtain tractable numerical or analytical solutions in each scenario are numerous and restrictive. As a result, the comparison of analytical results with numerical solutions still raises some issues (Salomons, 2000).

Hence, there is a need for a modeling solution valid at all scattering angles, in the presence of complex boundary conditions and atmospheric fluctuations, for generic acoustic signals. As argued by Ostashev *et al.* (2005), a set of two

[a]Author to whom correspondence should be addressed. Electronic mail: sylvain.cheinet@isl.eu

 0001-4966/2012/132(4)/2198/12/$30.00

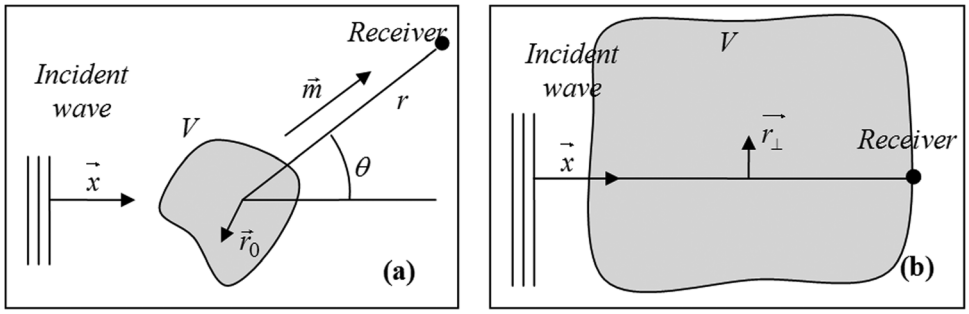

FIG. 1. Idealized sketches of the considered scattering geometries. In the large-angle geometry (a), the pressure field is considered outside and far from the shaded scattering volume. In the line-of-sight geometry (b), it is considered within the scattering volume and near the propagation axis of the incident wave.

coupled equations for the sound pressure and vector acoustic velocity can be solved with the finite difference time domain (FDTD) method, and provides such a versatile framework. The potential of this approach has been recognized and established in the last decade. It has for example been shown that it can ingest complex atmospheric fields (Symons *et al.*, 2004; Wilson and Liu, 2004; Cheinet and Naz, 2006). However, it remains to be demonstrated that it reliably estimates the effects of turbulence on sound propagation.

In particular, a well-posed issue is whether this approach is capable of reproducing the analytical results of T61. The considered set of equations includes the above Helmholtz-type equation as a special case. But numerical solutions may have errors and sometimes instabilities. Besides, contrary to the analytical solutions of T61, the statistical representativeness of the simulations of through turbulence has to be approximated. Last, the numerical simulation of turbulent fields is also limited compared to the analytical forms used in T61, if only by the finite domain size and spatial resolution of the computational domain.

The present study is intended to address this issue. It carefully investigates the performance of a FDTD solution for the two coupled equations in capturing the turbulent effects as predicted by T61. It is composed as follow. Section II introduces and evaluates the FDTD simulations in non-turbulent, previously documented propagation cases. Sections III and IV compare the FDTD predictions against the analytical results of T61 in the large and small scattering angle cases, respectively. In each case, the major assumptions and steps in the analytical derivations are presented. This comprehensive presentation, with consistent notations, highlighted common points and distinctive features, is a secondary, didactic purpose of this study. In these lines, Sec. V discusses the consistency of the large- and small-angle scattering approaches. Section VI summarizes the results.

II. DESCRIPTION OF THE MODELS

A. FDTD model

This section describes the FDTD model used in this study (see also Cheinet and Naz, 2006). The FDTD calculations are based on a set of two coupled equations for the sound pressure p_a and the acoustic velocity $\vec{w}_a$ in the atmosphere

$$\frac{\partial \vec{w}_a}{\partial t} = -(\vec{v}\cdot\vec{\nabla})\vec{w}_a - (\vec{w}_a\cdot\vec{\nabla})\vec{v} - \frac{\vec{\nabla}p_a}{\rho} + \frac{\vec{\mathrm{F}}}{\rho}, \tag{1}$$

$$\frac{\partial p_a}{\partial t} = -(\vec{v}\cdot\vec{\nabla})p_a - \rho c^2\vec{\nabla}\cdot\vec{w}_a + \rho c^2 Q, \tag{2}$$

where $\vec{\mathrm{F}}$ and Q account for force and mass sources, respectively. The atmospheric conditions are felt in Eqs. (1) and (2) through the wind velocity $\vec{v}$, density ρ, and sound speed c. As discussed by Ostashev *et al.* (2005), this set of equations is derived from the linearized system of fluid-dynamic equations by ignoring terms proportional to the divergence of the medium velocity and the gradient of the ambient pressure. This set of equations is more general than the equations used in previous analytical and numerical approaches to sound propagation through turbulence [see, e.g., Eq. (10)]. In particular, no approximation is made on the geometry of the propagation problem.

To the first order, ρ and c depend on the atmospheric pressure P, temperature T, and specific humidity q_t as [Ostashev, 1997, Eq. (6.23)]

$$\rho = \frac{P}{RT(1+0.61q_t)}, \tag{3}$$

$$c^2 = \gamma_{\mathrm{dry}}RT(1+0.51q_t). \tag{4}$$

Here the dry air characteristics are the gas constant R, specific heat capacity at constant volume C_v and the ratio $\gamma_{\mathrm{dry}} = (C_v+R)/C_v$.

Perfectly reflecting (rigid) surfaces (ground, obstacles, computational domain boundaries) are modeled with the method of images following Wilson and Liu (2004). Acoustically porous media can also be accounted for. Wilson and Liu show that a porous medium with an artificially small static flow resistivity acts as an absorbing boundary layer, which avoids reflection of the waves. The corresponding propagation equations are

$$\frac{\partial \vec{w}_a}{\partial t} = -\frac{\sigma}{\rho}\vec{w}_a - \frac{\vec{\nabla}p_a}{\rho}, \tag{5}$$

$$\frac{\partial p_a}{\partial t} = -\rho c^2\vec{\nabla}\cdot\vec{w}_a, \tag{6}$$

with the resistivity σ such that $\sigma/(\omega\rho) \ll 1$ for the angular frequency ω considered.

The FDTD model solves the above time-domain system for a given source and environment in two dimensions, denoted x and z. The prognostic variables are incremented in time by solving Eqs. (1), (2), (5), and (6) at each time step on the gridded computational domain. The algorithmic

choices in the present model are motivated by the careful discussions of Wilson and Liu (2004) and Ostashev *et al.* (2005). Specifically, the grid is taken equidistant with a half-level staggering of the velocity components. The spatial derivatives are approximated with second-order centered finite differences. Hereafter the grid-spacing Δx is typically chosen as one twentieth the signal wavelength. A fourth-order Runge–Kutta time integration is used. In the following simulations, the time-step Δt is chosen so that the Courant number $c\Delta t/\Delta x$ typically amounts to 0.65.

In the present study, only monochromatic sources are considered. Unless stated otherwise, the amplitude $|p|$ is taken as the maximum of the model pressure over one time period. This diagnostic is performed when the simulations have reached a stationary behavior, i.e., all significant forward and backward propagating contributions are accounted for. Hereafter the transmission loss TL (in dB) is defined as $\mathrm{TL} = 20\log_{10}(|p|/\tilde{p}_0)$, where $\tilde{p}_0$ is the pressure amplitude at the source.

B. Evaluation of the FDTD model

The present section is intended to evaluate the FDTD model in absence of turbulence. Simulation of sound propagation through turbulence, which is the main topic of this study, will be extensively dealt with in the next sections.

As a first test, a perfectly reflecting surface is considered over a homogeneous atmosphere. The point source emits at the frequency 100 Hz and height 19.5 m above the surface. The model's spatial resolution is 0.163 m and the time-step is 0.3 ms. Comparing with a known analytical solution [Wilson and Liu, 2004, Eq. (85)], the FDTD model reproduces the interference pattern between the direct and reflected contributions [Fig. 2(a)]. The inclusion of a wind vertical gradient ($|\vec{v}| = \mu z$ with $\mu = 1\,\mathrm{s}^{-1}$) induces some sound refraction [Fig. 2(b)]. The model prediction compares well with the analytical and numerical results of Ostashev *et al.* (2005). (Ostashev *et al.* mention that $z = 20$ m is used, but their results are more compatible with the present selection.)

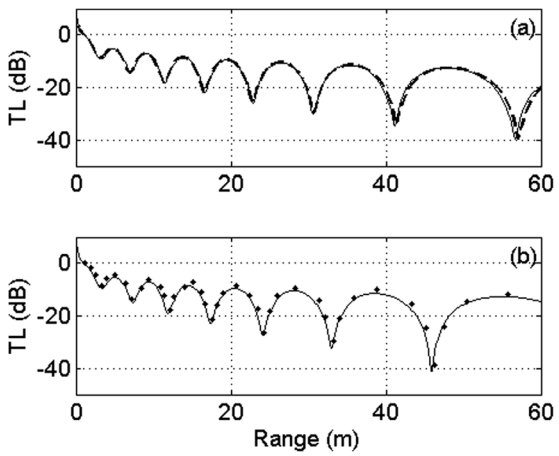

FIG. 2. Sound transmission loss (TL) with range along a horizontal line from the source, (a) without wind, in the FDTD simulation (solid line) and according to analytical results (dashed), and (b) with a vertical wind gradient, in the FDTD model (solid line) and after Ostashev *et al.* (2005) (symbols).

The second evaluation test is the propagation in presence of a prescribed wind vortex. This idealized test case is often considered in sound propagation modeling (e.g., Candel, 1979, Dallois and Blanc-Benon, 2001). Colonius *et al.* (1994) investigate the issue with a direct numerical solution (DNS). DNS integrates the complete set of coupled acoustic-fluid dynamics equations; it is thus more general and more computationally intensive than the present FDTD model. The scenario considered here follows one case analyzed by Colonius *et al.* (1994). The vortex azimuthal velocity is zero, the magnitude of the radial velocity is given by

$$v_\theta = \frac{\Gamma}{2\pi r}\left(1 - \exp\left(-\frac{\alpha r^2}{L^2}\right)\right), \tag{7}$$

with r the radial distance to the vortex core, $\alpha = 1.26$ and $L = 1$ m. The circulation Γ is taken as $\Gamma = 2.8\pi L c_0 M$, with $c_0 = 340\,\mathrm{m\,s}^{-1}$ a reference sound speed and $M = 0.125$ the Mach number. The incident plane wave is generated at a distance of 40 m at the left from the vortex center (Colonius *et al.*, 1994, find that this distance is of impact to the results). It has a frequency of 43 Hz. The simulation uses a spatial step of 0.1 m and a time-step of 0.2 ms, with 1001×1601 grid points.

Following Colonius *et al.*, the relative acoustic pressure perturbation is defined as the sound pressure minus the incident plane wave, normalized by the amplitude at the source. Figure 3 shows the angular dependence of this relative pressure perturbation at the range 4λ. The model prediction is in excellent agreement with the solution of Colonius *et al.* (1994). This agreement confirms the ability of the present FDTD model in simulating the sound propagation in this convective–refractive situation.

The model has also been tested in presence of diffractive obstacles (Ehrhardt and Cheinet, 2010). In the considered scenario, a point source emits at 50 Hz. It is located at a height of 25 m above a rigid ground, with a 40 m-high rigid barrier located 25 m to its right. The predicted sound levels behind the barrier are in excellent agreement with analytical expressions with range [Fig. 4(a)] and with height [Fig. 4(b)].

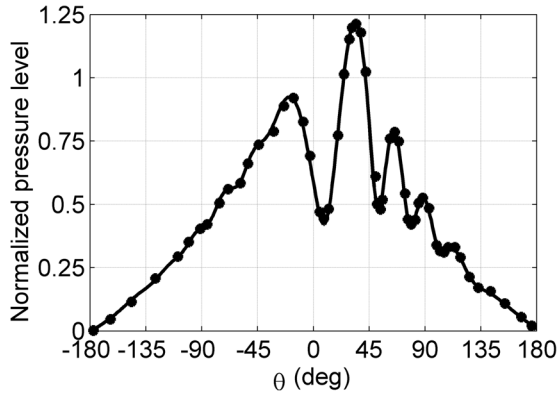

FIG. 3. Relative pressure scattered by a wind vortex at the range 4λ, in the FDTD model (solid line) and after Colonius *et al.* (1994) (circles, from dotted line in his Fig. 10).

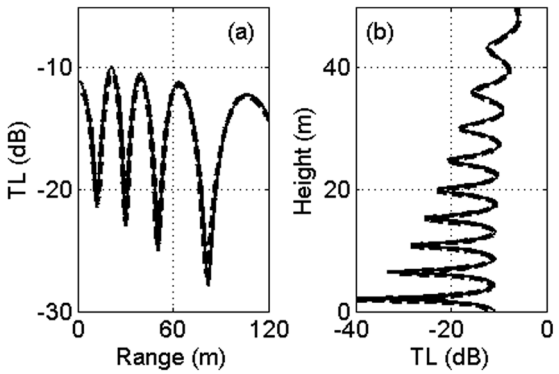

FIG. 4. Sound transmission loss (TL) behind a 40 m-high rigid barrier over a rigid surface, (a) along a horizontal line at the height $z = 20$ m and (b) on the vertical at the distance $x = 30$ m from the barrier, in the FDTD simulation (solid lines) and according to analytical results (dashed lines). The reference pressure level is taken at 1 m at the right of the barrier top.

C. Turbulent fluctuations modeling

This section introduces the methodology to achieve a compatible description of the turbulence fluctuations in the FDTD model and in the analytical approaches of T61.

Let s be a random scalar field and $\langle\rangle$ denote an ensemble average. Let $\vec{r}$ and $\vec{r}_0$ be some position vectors. The auto-correlation function is $B_s(\vec{r}_0, \vec{r}) = \langle s'(\vec{r}_0)s'(\vec{r}_0 + \vec{r})\rangle$ with $s' = s - \langle s\rangle$. The three-dimensional (3D) spectral density (or spectrum) of s, noted $\Phi_s^{3D}(\vec{r}_0, \vec{\kappa})$, is the Fourier transform of $B_s(\vec{r}_0, \vec{r})$ at vector wavenumber $\vec{\kappa}$. The dependence on $\vec{r}_0$ can be omitted under the assumption of homogeneous turbulence. Isotropic turbulence further implies that the dependence is only on the eddy wavenumber modulus κ.

The analytical approach to propagation focuses on particular statistical moments of the pressure field (e.g., T61). It analytically derives these moments in terms of the spectra of the thermodynamic quantities, on the underlying assumption that these spectra are well-behaved in the propagation medium. In the present study, only temperature fluctuations in a two-dimensional propagation medium are considered. The parameterization of the two-dimensional spectrum Φ_T^{2D} is now discussed.

Investigations of spectra in the near-surface atmosphere show three notable features (Panofsky, 1969; Kaimal, 1973; Kaimal, 1978; Andreas, 1987). (1) Spectra show a maximum at a certain wave-number, the corresponding length scale is hereafter denoted $L_{\max}$. (2) In the region $\kappa \gg 2\pi/L_{\max}$, the assumption of homogeneous and isotropic fluctuations is approximately verified, and the observed spectral dependence in $\kappa^{-11/3}$ agrees with the inertial-convective range theory. (3) In the region $\kappa < 2\pi/L_{\max}$ (large-scale eddies), the homogeneous and isotropic fluctuations assumption is doubtful (T61, p. 263). The propagation features caused by large-scale eddies still challenge the atmospheric acoustics community (Kallistratova, 2002).

It is recognized that near-surface atmospheric turbulence often features height dependence and intermittency (e.g., Cheinet *et al.*, 2011; Cheinet, 2012). Yet the above physical results allow introducing a relatively simple, physically-based spectrum. Specifically, a two-dimensional von Karman spectrum is used for temperature fluctuations [Hinze, 1959, Eq. (3.134)]

$$\Phi_T^{2D}(\kappa) = \frac{1}{2\pi\kappa}\frac{8\Gamma(17/6)}{3\sqrt{\pi}\Gamma(1/3)}\sigma_T^2\frac{\kappa^4 L_0^5}{(1+\kappa^2 L_0^2)^{17/6}}, \tag{8}$$

with L_0 a characteristic length scale and σ_T^2 the temperature variance. The maximum of Eq. (8) gives $L_{\max} = 2^{5/2}\pi L_0/3 \approx 5.92 L_0$. Equation (8) converges toward a $-8/3$ power law at large wave-numbers, as expected from the 2D inertial-convective range theory. The convergence toward zero at low κ gives that very large eddies negligibly contribute to the variance.

The purpose of our study is to compare the analytical results and the FDTD simulations for the same turbulence characteristics. The ensemble-averaged characterization with Eq. (8) is well-suited for the analytical approach of T61. But the FDTD model handles sound propagation in a deterministic manner, i.e., it predicts the 2D pressure field for a particular realization of the fluctuations in the medium.

In order to circumvent this issue, a model has been developed which uses Eq. (8) as input sampling function and sorts some random two-dimensional realizations of the atmospheric fluctuations. This model follows Frehlich *et al.* (2001). Each realization is obtained by discretizing the fluctuations spectrum, projecting with random phases and Fourier transforming to obtain the fluctuations in the physical space. The spectral grid is selected so that the physical grid of the fluctuations matches the FDTD model grid. In particular, the highest resolved wavenumber is taken as 2π divided by the spatial resolution of the FDTD model, and the lowest resolved wave-number is taken as 2π divided by the domain width of the FDTD model.

The FDTD model is then used to simulate sound propagation through each turbulence realization (Chevret *et al.*, 1996). This approach yields the probability distribution of the pressure field. The statistical moment of order n is evaluated from

$$\langle p_a^n(\vec{r})\rangle = \frac{1}{N}\sum_{i=1}^{N} p_{a,i}^n(\vec{r}), \tag{9}$$

with $p_{a,i}$ the FDTD pressure field predicted with the i-th turbulence realization. For the cases considered in this study, $N = 200$ random realizations are required in order to obtain a satisfactory convergence of the first- and second-order moments ($n = 1, 2$).

III. LARGE SCATTERING ANGLE

A. Analytical results

For a monochromatic wave outside the sources, one may cast the system of Eqs. (1) and (2) in a single second-order equation on the acoustic pressure. Let k denote the local wave-number, λ the wavelength and ω the angular frequency. The time dependence is extracted by introducing $p_a = pe^{-i\omega t}$ with p complex. The principle of the derivation is to take the divergence of Eq. (1), and substitute the result in the equation obtained by applying $\partial/\partial t$ to Eq. (2). Assuming that $\vec{\nabla}\cdot\vec{v} = 0$ and that the Mach number is small, the result is [e.g., Ostashev, 1994, Eq. (2)]

$$(\nabla^2 + k_0^2)p + \underbrace{\left[k_0^2\varepsilon - \vec{\nabla}\left(\ln\frac{\rho}{\rho_0}\right)\cdot\vec{\nabla}}_{R1\quad L1\quad R2} + \underbrace{2i\frac{k_0}{c_0}\vec{v}\cdot\vec{\nabla}}_{L2} - \underbrace{\frac{2i}{\omega}\frac{\partial v_i}{\partial x_j}\frac{\partial^2}{\partial x_i\partial x_j}}_{R3}\right]p = 0. \tag{10}$$

Here the subscript 0 indicates a reference value, and ε is defined by $\varepsilon = c_0^2/c^2 - 1$. First-order atmospheric perturbations (subscript 1) yield $\varepsilon = -T_1/T_0 - \eta_c q_1$ and $\ln(\rho/\rho_0) = -T_1/T_0 + \eta_\rho q_1$, with $\eta_c \approx 0.501$ and $\eta_\rho \approx -0.596$ (Ostashev, 1997, p. 171).

The above second-order, Helmholtz-type equation is obtained from Eqs. (1) and (2). Its solutions are thus included in the solutions of the FDTD model. This equation is the starting point of T61 and of many other analytical and numerical approaches to outdoor sound propagation. An equivalent form exists with $L2 + R3$ written as $-(2i/\omega)(\partial^2/\partial x_i\partial x_j)\{v_i(\partial p/\partial x_j)\}$ (Clifford and Brown, 1970; Candel, 1979). The operator in the square brackets in Eq. (10), hereafter denoted F, holds the environmental fluctuations.

The next major step in the classical theory is a small perturbation analysis. Under the Born approximation, p is written as a series $p = p_0 + p_1 + p_2 + \cdots$, and Eq. (10) is split over increasing orders with $p_0 \gg p_1 \gg p_2$. The zero-th order equation gives free field propagation. For an incident plane wave propagating in the direction $\vec{x}$, one has $p_0(\vec{r}) = \tilde{p}_0 \exp(ik_0\vec{x}.\vec{r})$. The first-order equation for p is

$$(\nabla^2 + k_0^2)p_1 + Fp_0 = 0. \tag{11}$$

Equation (11) uses the unperturbed wave p_0 as the exciting driver of the scattered wave p_1; it is a single-scattering approximation. Its three-dimensional solution is

$$p_1(\vec{r}) = \frac{1}{4\pi}\iiint_V \frac{e^{ik_0|\vec{r}-\vec{r'}|}}{|\vec{r}-\vec{r'}|}Fp_0(\vec{r'})d^3\vec{r'}, \tag{12}$$

with V the scattering volume.

The analytical derivations of scattering effects at large versus small angles diverge on the geometrical approximations in the subsequent treatment of Eq. (12). Let $\vec{r} = (r, \theta, \phi)$ in spherical coordinates with r the magnitude of $\vec{r}$, θ the polar angle oriented from the x-axis, and φ the azimuth angle. In the large scattering angle scenario, the acoustic field is considered at r large compared to the characteristic length H of the scattering volume. This far-field approximation gives

$$p_1(\vec{r}) = \frac{e^{ikr}}{4\pi r}\tilde{p}_0 k_0^2 \iiint_V f(\vec{r}_0)e^{i\vec{\kappa}.\vec{r}_0}d^3\vec{r}_0, \tag{13}$$

with $\vec{\kappa} = k_0(\vec{x} - \vec{m})$, $\vec{m} = \vec{r}/r$, and $f(\vec{r}) = \varepsilon(\vec{r}) - (1 - \cos\theta)\ln(\rho(\vec{r})/\rho_0) - 2\cos(\theta)v_x(\vec{r})/c_0$. The large-volume approximation further assumes that H is much larger than the characteristic scale of the turbulent fluctuations (T61, pp. 66–68). Extending the integration to infinity in Eq. (13) leads to a Fourier transform of the spatial distribution of f at the wavenumber $\vec{\kappa}$.

To relate this Fourier transform to the atmospheric spectra, one can introduce the intensity $I_1(\vec{r}) = p_1(\vec{r})p_1^*(\vec{r})$. Here the star denotes the complex conjugate. For homogeneous, isotropic, non-divergent fluctuations, $\langle I_1\rangle$ may be written in terms of the three-dimensional spectra of temperature, specific humidity, temperature-humidity, and turbulent kinetic energy, noted Φ_T^{3D}, Φ_q^{3D}, $\Phi_{T,q}^{3D}$, and E^{3D}. Specifically, $\langle I_1\rangle$ does not depend on the longitudinal angle φ, it is given by [Ostashev, 1997, Eq. (7.12)]

$$\langle I_1(r,\theta)\rangle = I_0\frac{V}{r^2}2\pi k_0^4\left\{\frac{\beta^2\Phi_T^{3D}(\kappa(\theta))}{4T_0^2} + \frac{\eta^2\Phi_q^{3D}(\kappa(\theta))}{4} + \frac{\eta\beta\Phi_{T,q}^{3D}(\kappa(\theta))}{2T_0} + \frac{\nu E^{3D}(\kappa(\theta))}{c_0^2}\right\}, \tag{14}$$

with $I_0 = \tilde{p}_0^2$, $\beta = 1 - 2\sin^2(\theta/2) = \cos(\theta)$, $\eta = \eta_c + 2\eta_\rho\sin^2(\theta/2)$, and $\nu = \cos^2(\theta)\cos^2(\theta/2)$. The first term on the right hand side (RHS) inside the brackets in Eq. (14) is caused by temperature fluctuations, which modulate both the sound speed ($L1$) and the density ($R2$). Comparably, the last RHS term is caused by the wind-related effects ($L2$ and $R3$). According to Eq. (14), $\langle I_1(r,\theta)\rangle$ depends on the fluctuations of size

$$l(\theta) = 2\pi/\kappa(\theta) = \lambda/\Big(2\sin(\theta/2)\Big), \tag{15}$$

The scattering angle decreases with the eddy size.

B. Comparison FDTD model—analytical results

The above analytical results are now compared to the FDTD model predictions for scattering from a disk with enclosed temperature fluctuations. Because the latter use a 2D configuration, Eq. (14) is first expressed in this context. Additionally, as the model is tested with temperature fluctuations only, the expression is simplified accordingly. Under the small perturbations approximation, the 2D pressure field writes as

$$p_1(\vec{r}) = \frac{i}{4}\tilde{p}_0\iint_S H_0(k_0\|\vec{r}_0 - \vec{r}\|)\left[k_0^2\varepsilon - \vec{\nabla}\left(\ln\frac{\rho}{\rho_0}\right)\cdot\vec{\nabla}\right] \times e^{ik_0\vec{x}.\vec{r}_0}d^2\vec{r}_0, \tag{16}$$

where S is the scattering surface and H_0 is the zero-th order Hankel function of the first kind. The far-field approximation leads to

$$p_1(\vec{r}) = \frac{e^{ik_0r + i(\pi/4)}}{\sqrt{8\pi k_0 r}}\tilde{p}_0 k_0^2\iint_S f(\vec{r}_0)e^{i\vec{\kappa}\cdot\vec{r}_0}d^2\vec{r}_0. \tag{17}$$

Under the large-volume approximation, the average scattered intensity is then given by [Cotté and Blanc-Benon, 2007, Eq. (A25)]

$$\langle I_1(r,\theta)\rangle = I_0 \frac{S}{r} 2\pi k_0^3 \left\{ \beta^2 \frac{\Phi_T^{2D}(\kappa(\theta))}{4T_0^2} \right\}, \tag{18}$$

with κ given by Eq. (15).

The considered test case is as follows. The computational domain is a square of 600 m × 600 m, with a spatial resolution of 0.25 m and a time-step of 0.5 ms. It includes 100 m-thick absorbing layers on the borders. A 50 Hz pressure wave is imposed along the right of the left-side absorbing layer. The background temperature is 295 K. The scattering surface is a disk of radius $H = 25$ m at the center of the domain. The temperature fluctuations within the disk are extracted from random fluctuations simulations with $L_{\max} = 15$ m and $\sigma_T = 1$ K (Sec. II C). A Tukey window (tapered cosine) is used at the disk boundaries to avoid discontinuities in the temperature field. The density and sound speed in the atmospheric domain are calculated from Eqs. (3) and (4).

The scattered wave p_1 is calculated as the difference between the pressure field simulated with and without turbulence. Figure 5 shows the scattering cross section $\sigma = I_1 r/(I_0 S)$ at a range of 200 m, for one turbulence realization. It shows large fluctuations with the scattering angle. The numerical integration of Eq. (16) is virtually identical to the FDTD simulation (not shown). The average scattering cross section $\langle\sigma\rangle$ converges with the $N = 200$ simulations considered here. The general agreement with the analytical result of Eq. (18) demonstrates the consistency between the FDTD simulations and the theory in the considered test case. It also shows that the large-volume approximation can provide realistic predictions despite the relatively low number of characteristic turbulent structures in the scattering area—given by $(2H/L_{\max})^2 \approx 11$.

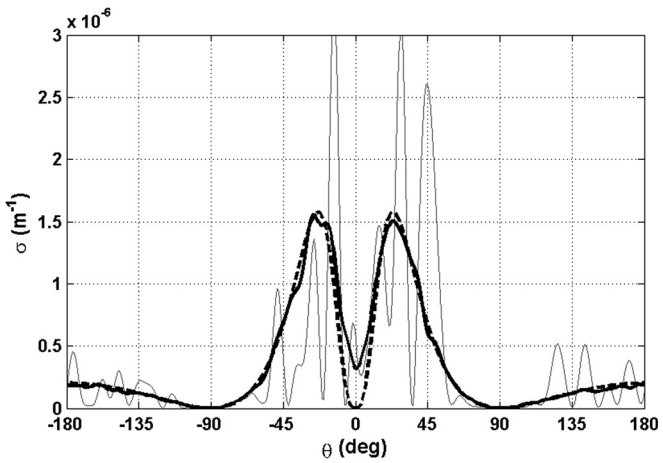

FIG. 5. Sound scattering cross section with the scattering angle θ at $r = 200$ m. The grey line is the FDTD model result for one particular realization of the turbulent fluctuations, the thick solid line is the average over 200 realizations. The analytical result for large scattering angle [Eq. (18)] is the thick dashed line.

The scattering cross section shows very small values at $\theta = \pm 90°$, both in the numerical and analytical results. Let ε_{eq} denote $\varepsilon - 2v_x/c_0$. Equation (13) yields $F = k_0{}^2\varepsilon_{\text{eq}} - ik_0(\vec{x}\cdot\vec{\nabla})\varepsilon_{\text{eq}}$ in the absence of humidity fluctuations (Candel, 1979). The first contribution in this expression relates to $L1$ and $L2$; the second relates to $R2$ and $R3$. In the large-volume approximation, the pressure scattered by the second contribution is $(\cos\theta - 1)$ times the pressure scattered by the first. Accounting for $R2$ and $R3$ thus induces a $\cos^2\theta$ factor on the intensity [T61, p. 259, see β^2 and ν in Eq. (14)]. $R2$ and $R3$, respectively, compensate $L1$ and $L2$ in the transverse directions, which explains the minima at $\theta = \pm 90°$. The FDTD model is capable of capturing this feature.

At $\theta \approx 0°$, the FDTD model still shows some significant scattering, while the analytical prediction is zero. The finite size of the scattering disk is not accounted for in Eq. (18), which requires $l(\theta) < H$ and is thus valid for $\theta > \sqrt{\lambda/r}$. As pointed by Daigle *et al.* (1986), the analytical solution is not applicable at small scattering angles for finite-size volumes (surfaces in 2D).

IV. SMALL SCATTERING ANGLE

In comparison with the large-angle scattering considered in Sec. III, the physical derivation can be made more specific when the scattering effects are concentrated in the forward direction. This is now discussed.

A. The small scattering angle approximation

Figure 6 shows the frequency dependence of the scattered acoustic intensity in Eq. (18)—the same behavior is obtained with Eq. (14). At low acoustic frequencies ($\lambda \gg L_{\max}$), the relevant eddies for scattering are outside the inertial-convective range [Eq. (15)]. In this region, the turbulence spectrum increases with the wave-number. There is more back-scattering than forward scattering. At high frequencies ($\lambda \ll L_{\max}$), the relevant eddies are in the inertial-convective range, where the spectrum decreases with the wave-number. The large-angle scattering becomes negligible compared to the forward scattering. At sufficiently high

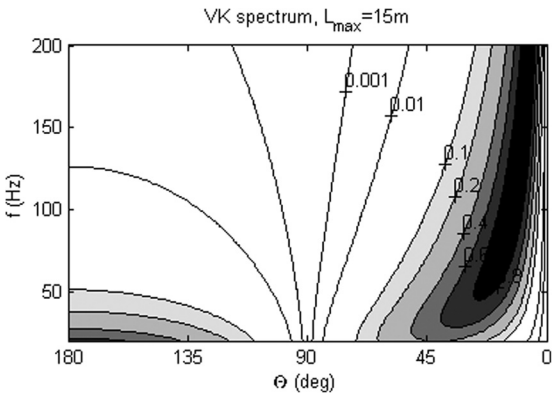

FIG. 6. Scattering cross section as a function of the scattering angle and acoustic frequency, according to Eq. (18) utilizing the von Karman spectrum of Eq. (8) with $L_{\max} = 15$ m and $\sigma_T = 1$ K. The values are normalized by the maximum at 200 Hz.

frequencies, the maximum scattering is approximately held by the eddies of characteristic size $L_{\max}$ and is at the angle

$$\theta_{\max} = 2\arcsin\left(\frac{\lambda}{2L_{\max}}\right). \tag{19}$$

The small scattering angle approximation assumes that the scattering effects are concentrated within a cone of small angular aperture in the forward direction. It thus uses $\theta_{\max} < 1$. From Eq. (19), it is equivalent to the high-frequency approximation $\lambda < L_{\max}$. This equivalence is quantitatively re-assessed in Sec. IV D. It is readily obtained here from the physical analysis of the large-angle scattering approach.

B. Analytical results

The analytical results obtained under the small-angle scattering approximation are now briefly recalled. Following the discussion of Sec. III B, $R2$ and $R3$ have no impact in the backward ($\theta = \pi$) and forward ($\theta = 0$) directions. Hence, they can be neglected under the small angle scattering approximation. The contribution of the transverse wind in $L2$ is also neglected (Ostashev, 1997, p. 194). One then obtains $F = k_0^2\varepsilon_{\text{eq}}$, where ε_{eq} was defined in Sec. III B. A paraxial (near-axis) approximation of Eq. (12) in the transverse direction can be introduced, with $\vec{r} = (L, \vec{r}_\perp)$. The result for $\psi_1 = p_1/p_0$ is [T61, Eq. (7.23), see also Strohbehn, 1968, Eq. (12)]

$$\psi_1(L,\vec{r}_\perp) = \frac{k_0^2}{4\pi}\int_0^L \iint_{S_\perp} \frac{e^{ik_0[(\vec{r}_\perp - \vec{r'}_\perp)^2/2(L-x)]}}{L-x}\varepsilon_{\text{eq}}(x,\vec{r'}_\perp)d^2\vec{r'}_\perp dx. \tag{20}$$

The real and imaginary parts of ψ_1 are hereafter denoted χ_1 and S_1.

The perturbation analysis is often introduced in a different form. Defining $p = \exp(\psi)$, the Rytov approximation uses $\psi = \psi_0 + \psi_1 + \psi_2 + \cdots$ with $\psi_0 \gg \psi_1 \gg \psi_2$. This mathematical treatment is also referred to as a smooth-perturbation approximation, in contrast to the above small-perturbation approximation. The first-order equation coincides with Eq. (20), so the major difference is in the interpretation of ψ_1 (McBride *et al.*, 1991): the Born and Rytov approximations respectively use the total pressure fields

$$p = p_0(1 + \psi_1), \tag{21}$$

$$p = p_0 \exp(\psi_1). \tag{22}$$

The expressions match in their common domain of validity, see Brownlee (1974), Clifford (1978), and Yura *et al.* (1983). Under the Rytov formalism, $\chi_1 \approx \ln(|p|/|p_0|)$ is the log-amplitude. This terminology is adopted in this section for it is more standard within the context of line-of-sight propagation studies.

A large-volume approximation again arises at this step. Extending the transverse integration toward infinity in Eq. (20), the spectral transform (denoted with tilde) of ψ_1 can be identified [e.g., T61, Eq. (7.37), Ostashev and Wilson, 2001, Eq. (22)]

$$\tilde{\psi}_1(L,\vec{\kappa}_\perp) = \frac{ik_0}{2}\int_0^L e^{-i[\kappa_\perp^2(L-x)/2k_0]}\tilde{\varepsilon}_{\text{eq}}(x,\vec{\kappa}_\perp)dx. \tag{23}$$

Equation (23) allows deriving the spectra Φ_χ and Φ_S of χ_1 and S_1 from the real and imaginary parts of $\tilde{\psi}_1$. Following the Markov approximation, the correlation in ε_{eq} in the x-axis direction is neglected. Then Φ_χ and Φ_S may be written in terms of $\Phi^{3D}_{\varepsilon_{\text{eq}}}$. Let $B_\chi(L,\vec{r}_\perp) = \langle\chi_1(L,\vec{r}_A)\chi_1(L,\vec{r}_B)\rangle$ and $B_S(L,\vec{r}_\perp) = \langle S_1(L,\vec{r}_A)S_1(L,\vec{r}_B)\rangle$ denote the transverse autocorrelation functions of χ_1 and S_1, with $\vec{r}_A$ and $\vec{r}_B$ in the transverse plane and $\vec{r}_\perp = \vec{r}_A - \vec{r}_B$. For isotropic perturbations, B_χ and B_S simply relate to Φ_χ and Φ_S, and one finally obtains [Lawrence and Strohbehn, 1970, Eq. (T21)]

$$B_\chi(L,r_\perp) = \pi^2 k_0^2\int_0^L\int_0^\infty \sin^2\left(\frac{\kappa^2(L-x)}{2k_0}\right)\Phi^{3D}_{\varepsilon_{\text{eq}}}(\kappa) \times J_0(\kappa r_\perp)\kappa\, d\kappa\, dx, \tag{24}$$

$$B_S(L,r_\perp) = \pi^2 k_0^2\int_0^L\int_0^\infty \cos^2\left(\frac{\kappa^2(L-x)}{2k_0}\right)\Phi^{3D}_{\varepsilon_{\text{eq}}}(\kappa) \times J_0(\kappa r_\perp)\kappa\, d\kappa\, dx. \tag{25}$$

These equations still apply in presence of large-scale heterogeneities in turbulence characteristics, as is felt through, e.g., the dependence of the spectrum $\Phi^{3D}_{\varepsilon_{\text{eq}}}$ on x. They can be used to quantify the transverse de-correlation of the signal due to turbulence. Specifically, from Eq. (22), the transverse second-order moment is given by

$$\frac{\langle p(L,\vec{r}_A)p(L,\vec{r}_B)^*\rangle}{I_0} = \exp\Big(-\{B_\chi(L,0) - B_\chi(L,r_\perp) + B_S(L,0) - B_S(L,r_\perp)\}\Big). \tag{26}$$

With $r_\perp = 0$, Eqs. (24) and (25) give the variances of the log-amplitude and phase fluctuations due to the turbulence. In this case, Eq. (26) also predicts that the total acoustic intensity $I_{\text{tot}} = \langle pp^*\rangle$ is constant with range, and amounts to the value without turbulence I_0. This result is expected, since only forward scattering takes place. Conversely, for large $r_\perp$, the two points are uncorrelated, and Eq. (26) gives

$$\frac{\langle p(L,r_A)\rangle\langle p^*(L,r_A)\rangle}{I_0} = e^{-\gamma L}, \tag{27}$$

with the attenuation coefficient given by

$$\gamma = \frac{B_\chi(L,0) + B_S(L,0)}{L} = \pi^2 k_0^2\int_0^\infty \Phi^{3D}_{\varepsilon_{\text{eq}}}(\kappa)\kappa d\kappa. \tag{28}$$

C. Comparison FDTD model—analytical results

Comparison between FDTD model and analytical results is again performed in the context of two-dimensional propagation. The equation for ψ_1 corresponding to Eq. (20) is

$$\psi_1(\vec{r}) = k_0^2\frac{i}{4}\int\int H_0(k_0|\vec{r}_0 - \vec{r}|)e^{ik_0(\vec{r}_0 - \vec{r})\cdot\vec{x}}\varepsilon_{\text{eq}}(\vec{r}_0)d^2\vec{r}_0. \tag{29}$$

The further simplification of this expression requires a far field approximation of the Hankel function H_0. The rest of the derivation follows the 3D case. As a result, one obtains

$$B_\chi(L, r_\perp) = \frac{\pi}{2} k_0^2 \int_0^L \int_0^\infty \sin^2\left(\frac{\kappa^2 (L-x)}{2k_0}\right) \Phi_{\varepsilon_{\rm eq}}^{\rm 2D}(\kappa) \times \cos(\kappa r_\perp) d\kappa dx. \quad (30)$$

$$B_S(L, r_\perp) = \frac{\pi}{2} k_0^2 \int_0^L \int_0^\infty \cos^2\left(\frac{\kappa^2 (L-x)}{2k_0}\right) \Phi_{\varepsilon_{\rm eq}}^{\rm 2D}(\kappa) \times \cos(\kappa r_\perp) d\kappa dx. \quad (31)$$

These expressions differ from Eqs. (24) and (25) by the cosine replacing the Bessel function in the integrand. This change may not appear if one replaces the 3D spectrum with the 2D spectrum times the delta function in the third dimension (Salomons, 2000).

The considered test case is as follows. The computational domain is a rectangle of 408 m × 120 m. On the left is a 84 m-thick absorbing layer. A 100 Hz pressure wave is imposed along its right. The FDTD model spatial resolution is 0.12 m, the time-step is 0.2 ms. The temperature in the 324 m-thick turbulent domain has a mean of 295 K, with random fluctuations produced with $L_{\max} = 30$ m and $\sigma_T = 1$ K. The density and sound speed in this domain are calculated from Eqs. (3) and (4). The domain of analysis has a width of 240 m. The remaining 84 m-thick layer on the right allows reaching a stationary state and avoids the perturbations from the right boundary. The upper and lower boundary conditions are periodic. This infinite extension of the turbulent medium in the transverse direction agrees with the large-volume approximation made to derive the analytical results [Eq. (23)]. The transverse dimension of the computational domain is large enough to avoid any alteration of the results by the periodicity of the turbulent medium (see below). The local amplitude and phase are obtained by Fourier-transforming the FDTD pressure over a time period at the source frequency. The statistics at each range are evaluated from Eq. (9) with $N = 1024$ simulations, augmented with a sampling along the transverse direction.

Figures 7(a) and 7(b), respectively, show the range-dependences of the variances of log-amplitude and phase and of the mean pressure field. The analytical solutions in Fig. 7(a) are given by the right-hand side terms of Eqs. (30) and (31) with $r_\perp = 0$. Figure 7(b) uses the square root of the right-hand side term of Eq. (27). For the FDTD model, the variances increase and the mean pressure field is attenuated with range, in quantitative agreement with the analytical predictions. At long ranges, the phase and log-amplitude variances tend to converge, as expected from theory (e.g., Flatté *et al.*, 1979, Fig. 8.7). The log-amplitude variance (sometimes referred to as the Rytov's parameter) remains much smaller than one, i.e. the pressure fluctuations remain much smaller than p_0 (smooth perturbations). At short ranges, the log-amplitude variance is much smaller than the phase variance. This corresponds to the geometrical optics regime in the sense of Flatté *et al.* (1979), defined such that $\sqrt{\lambda L} \ll L_{\max}$. Other authors (e.g., Strohbehn, 1968) define

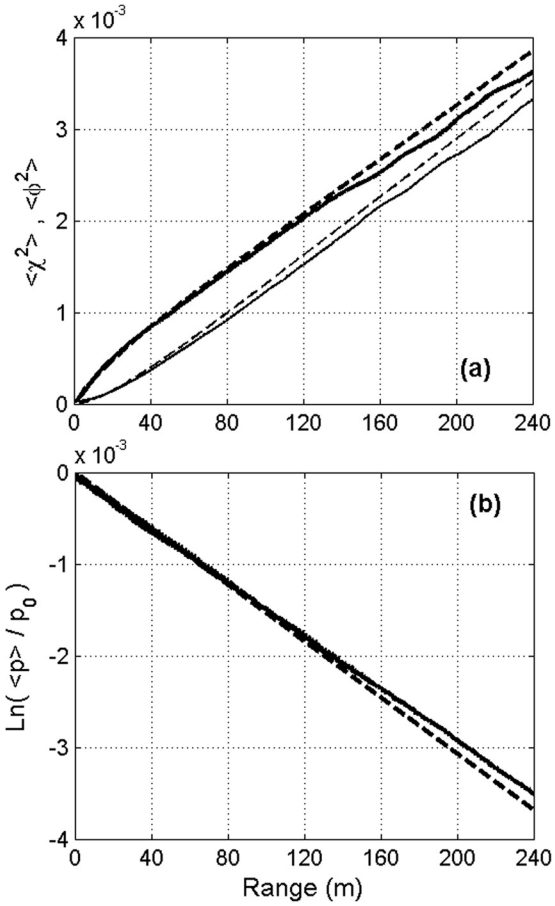

FIG. 7. Comparison between the FDTD model predictions (solid line) and the analytical results for small scattering angle (dashed) with the propagation range, (a) for the variances of log-amplitude (thin lines) and phase (thick) and (b) for the normalized amplitude of the mean pressure field.

the geometrical optics regime with a more stringent criterion, i.e., $\sqrt{\lambda L} \ll L_{\min}$, with $L_{\min}$ an inner scale below which there are no turbulent fluctuations. With $L_{\min} \propto \Delta x$, this regime is at too short ranges to be resolved in our simulations.

Figure 8 shows the transverse coherence with range. The FDTD model result is the left-hand side term in Eq. (26); the analytical result is the right-hand side term. The coherence is periodic in the model predictions given the periodic boundary conditions. The domain aspect ratio (width/length) is large enough to maintain the independence of each side. The coherence decreases with range as turbulence decorrelates the signal. It remains small; a large de-coherence would imply a strong attenuation of $\langle p \rangle$ and the smooth-perturbation approximation would fail. The FDTD model prediction agrees fairly well with the analytical result, which again gives a check of both.

D. The small-scattering angle approximation for PE approaches

The analytical derivations in Sec. IV B start from the smooth-perturbation approximation of Eq. (10), namely, Eq. (12), and then introduce the small scattering angle approximation. In the acoustic research literature, the small scattering angle approximation is often used first, to reduce Eq. (10) to a parabolic equation [Candel, 1979; Ostashev, 1997,

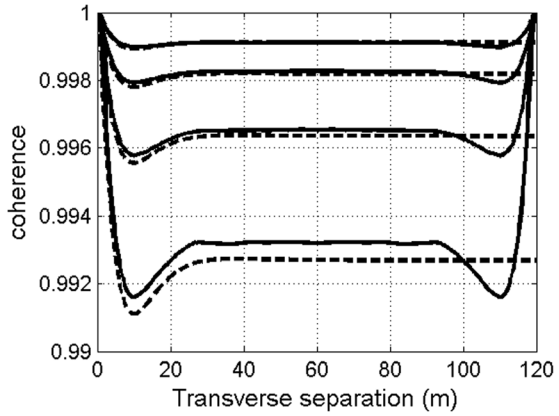

FIG. 8. Comparison between the FDTD model predictions (solid line) and the analytical result for small scattering angle (dashed) for the transverse coherence length, at four ranges, from top to bottom: 30, 60, 120, and 240 m. The periodic domain of the FDTD model causes its symmetric prediction.

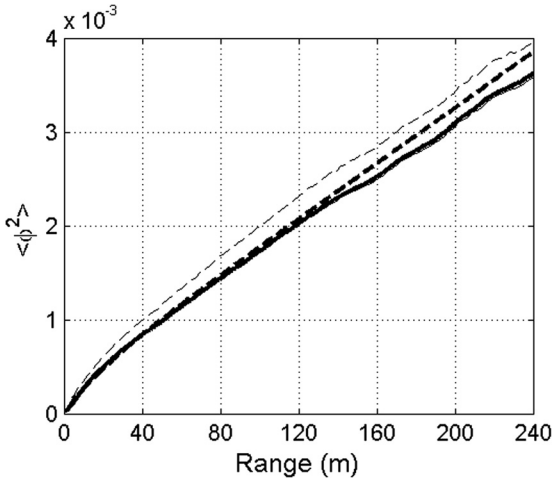

FIG. 9. Variance of phase with range, predicted with the FDTD model (thick solid line), the numerical integration of Eq. (16) (thin solid line, hardly distinguishable from the FDTD model prediction), the same integration without the term due to $R2$ (thin dashed) and the analytical result for small scattering angle (thick dashed).

Eq. (7.25)]. Specifically, one has $F = k_0^2 \varepsilon_{\text{eq}}$ under the small scattering angle approximation (Sec. III B), so Eq. (10) takes the form

$$(\nabla^2 + k_0^2)p + k_0^2 \varepsilon_{\text{eq}} p = 0. \tag{32}$$

Under the paraxial approximation, Eq. (32) takes the PE form [e.g., T61, Eq. (7.24)]

$$2ik_0 \frac{\partial p}{\partial x} + \nabla_\perp^2 p + k_0^2 (2 + \varepsilon_{\text{eq}}) p = 0. \tag{33}$$

Equation (33) leads to the same results as in Sec. IV B, Eqs. (24) and (25), under the smooth-perturbation and Markov approximations. The interest of Eq. (33) is that it can also be solved numerically, without recourse to the smooth perturbation approximation.

Whatever the solution of the PE is, analytical or numerical, it is obtained under the small scattering angle approximation. Let θ_{PE} denote the angular limitation for a given PE approach (e.g., Jensen *et al.*, 2000, p. 337). The PE approach and the small scattering angle approximation are compatible if $\theta_{\text{PE}} > \theta_{\max}$ or

$$\frac{\lambda}{L_{\max}} < 2 \sin(\theta_{\text{PE}}/2). \tag{34}$$

This equation states that the acoustic frequency must be sufficiently high for the dominant scattering to be within the PE-resolved angular cone. It is a prerequisite to using the PE approach through turbulence. For example, the paraxial parabolic equation [Eq. (33)] has $\theta_{\text{PE}} \approx 20°$ (Jensen *et al.*, 2000). It is applicable if $\lambda/L_{\max} < 0.35$.

In Sec. IV C, one has $\lambda/L_{\max} \approx 0.11$. The small scattering angle approximation is fulfilled and the paraxial PE approach is applicable, i.e., the analytical results of Sec. IV B are valid. However the impact of $R2$ may still be examined—recall that $R3 = 0$ in the test case. Figure 9 shows the numerical integration of Eq. (16), i.e., with $R2$ accounted for. It is in excellent agreement with the FDTD model. The numerical integration without $R2$ slightly over-estimates the phase variance. The other assumptions in the theory tend to compensate the over-estimation. Overall, the over-estimation is expected, since the density effects ($R2$) do not compensate the sound speed effects ($L1$). This explains the minor but systematic tendency of the analytical solutions to over-predict the effects induced by turbulence compared to the FDTD model results shown in Figs. 7 and 8.

Salomons (2000) compares some PE simulations with the analytical solutions. The larger turbulent scales accounted for in his study are of the size $L_{\max} \approx 2$ m. For $\theta_{\text{PE}} \approx 30°$, a value representative of his models, the lower admissible frequency is 330 Hz. At lower acoustic frequencies, both these PE approaches and the analytical solutions of Sec. IV B are inapplicable since the scattering angles are too large. This result certainly explains the discrepancies reported by Salomons (2000, Fig. 4) at 125 and 250 Hz. It also illustrates the need of overcoming the PE limitations when low frequency sounds or propagation effects of turbulence with low $L_{\max}$ are investigated. Cheinet (2012, Sec. III B) investigates the practical implications of this limitation for PE simulations in the near-surface turbulent atmosphere.

The above angular limitation of the paraxial PE approach has led to the development of wide-angle PEs, with relaxed angular limitations and $R2$ and $R3$ accounted for (Ostashev *et al.*, 1997). However, the PE approach structurally ignores backscattering ($\theta > \pi/2$), and can represent scattering processes only if $\lambda/L_{\max} < \sqrt{2}$. This absolute condition is only slightly more relaxed than the model-specific Eq. (34).

The refractive term in Eq. (32) can be cast in the form $\varepsilon_{\text{eq}} = c_0^2/c_{\text{eff}}^2 - 1$, with $c_{\text{eff}} = c + v_x$ an effective sound speed. This shows that that the concept of an effective sound speed holds within the small scattering angle approximation, which has been written $\lambda < L_{\max}$. Whereas this high-frequency limitation is known to affect the PE approach, it is also met in other approaches based on an effective sound velocity, such as the transmission line matrix approach (e.g., Aumond *et al.*, 2010).

V. DISCUSSION

The large scattering angle and line-of-sight theories should provide a consistent view of the energy transfer from the incident to the scattered contributions. The present section addresses this aspect.

Following the Markov approximation, let's consider a succession of independent planar screens of infinitesimal thickness δx and of finite transverse section. The exciting pressure field for scattering within the screen located at range x is the mean coherent field $\langle p(x)\rangle$. Let $I(x) = \langle p(x)\rangle\langle p^*(x)\rangle$ be the associated intensity in the $\vec{x}$ direction. The large-angle scattering approach allows investigating the pressure field $\delta p_1(x,\vec{r})$ scattered by turbulence in the direction $\vec{r}$ by the screen at x. Averaging Eq. (13) shows that $\langle \delta p_1(x,\vec{r})\rangle = 0$, since $\langle \varepsilon\rangle$ is null with the appropriate reference values. Thus the only intensity contribution associated with scattering is through $\langle \delta I_1(x,\vec{r})\rangle = \langle \delta p_1(x,\vec{r})\delta p_1^*(x,\vec{r})\rangle$. In particular, the total scattered intensity is given by an integration of Eq. (14) over the differential element $2\pi r^2 \sin\theta d\theta$

$$\langle \delta I_1(x)\rangle = 4\pi^2 k_0^4 \delta x I(x)\int_0^\pi \Phi_n^{3D}\left(2k_0\sin\frac{\theta}{2}\right)\sin\theta d\theta, \tag{35}$$

where Φ_n^{3D} is the term in the curly brackets in the right-hand side of Eq. (14).

In this equation, the integration upper bound ($\theta = \pi$) corresponds to the eddy wave-number $2k_0$ and size $\lambda/2$. Assume that $\lambda < L_{\max}$. Then $\lambda/2$ is in the inertial-convective range, so the three-dimensional spectrum Φ_n^{3D} decreases beyond $2k_0$ typically in $\kappa^{-11/3}$. Hence the additional contribution induced by extending the integration upper bound to infinity negligibly alters the result. This extension yields the analytical solution $\langle \delta I_1(x)\rangle = \gamma_n I(x)\delta x$, where $\gamma_n = 4\pi^2 k_0^2 \int_0^\infty \Phi_n^{3D}(\kappa)\kappa d\kappa$. But the condition $\lambda < L_{\max}$ implies $\theta_{\max} < 1$ (small-angle approximation). In this case $R2$ and $R3$ can be neglected, $\Phi_n^{3D} = \Phi_{\varepsilon_{eq}}^{3D}/4$ and $\gamma_n = \gamma$, so one finally obtains

$$\langle \delta I_1(x)\rangle = \gamma I(x)\delta x. \tag{36}$$

The intensity attached with the mean out-coming pressure field, which is the exciting field for the next screen, may be evaluated from the budget equation $I(x+\delta x) + \langle \delta I_1(x)\rangle = I(x)$. This budget points out that turbulence scattering causes the transfer from the mean coherent pressure field to scattered pressure fluctuations. (The total intensity remains constant with range, as discussed in Sec. IV.) Integrating the above budget over the range $x = 0$ to $x = L$ with Eq. (36) leads to the exponential decrease of the mean pressure field, Eq. (27), obtained in the line-of-sight approach.

Note that Eq. (35), combined with the above budget, already produces an exponential decrease of the mean pressure field. This qualitative theoretical prediction holds whatever the scattering angle is, i.e., for all frequencies. The remainder of the above derivation shows that the characteristic length for this decrease takes the quantitative form $1/\gamma$ in the small scattering angle (high frequency) approximation, as expected from Sec. IV B. This demonstrates the consistency between the theoretical results of T61 in the small and large scattering angle cases within the appropriate approximations.

This consistency is discussed by T61 (pp. 156–163) with the terms $L2$, $R2$, and $R3$ neglected *a priori*. In effect, T61 also considers electro-magnetic propagation, since the Maxwell equations lead to an equation very similar to Eq. (10). The terms $L2$, $R2$, and $R3$ do not appear or are negligible in the electro-magnetic propagation counterpart. Besides, at optical wavelengths ($\lambda < 10^{-6}$ m), the high-frequency (small scattering angle) hypothesis is always fulfilled in the atmosphere (Strohbehn, 1968). The optical propagation meets other physical challenges, e.g., defining the turbulence spectrum at large wave-numbers.

VI. CONCLUSIONS

Many aspects of outdoor sound propagation strongly depend on atmospheric turbulence. The experimental characterization of these dependencies raises major difficulties. Standard complementary theoretical and numerical assessments of these effects make an *a priori* distinction between two scenarios, one for the line-of-sight propagation, the other for the scattering at large angles. This distinction stems from the approximations needed in order to obtain tractable equations.

This study presents the common and distinctive features for these solutions, in the case of an incident plane wave. The line-of-sight and large-scattering angle approaches both rely on a perturbation analysis. They also both require a large-volume approximation to relate the turbulent fluctuations to their spectrum. They both provide the mean scattered intensity and are shown to be consistent one with the other (Sec. V). Further analytical predictions are obtained on the variability of the scattered field in the line-of-sight case. This is at the expense of the Markov approximation and a small-scattering angle approximation. The latter is interpreted as a high-frequency requirement. In this perspective, the line-of-sight approach can be regarded as a high-frequency particular case of the more general, large scattering angle approach.

To overcome the above distinction, a set of two coupled equations for the acoustic pressure and the vector acoustic velocity can be numerically integrated in finite difference time domain (FDTD). The FDTD model considered in this study is a two-dimensional model which closely follows the description by Wilson and Liu (2004). It is shown to appropriately simulate the refractive/diffractive/convective effects in various non-trivial configurations. The comparative set-up uses some random realizations of the temperature fluctuations, which are generated from the considered von Karman spectrum. The FDTD model is used to numerically simulate the two-dimensional propagation of a plane wave through the generated turbulent fields within the geometrical assumptions corresponding to the analytical solutions. The statistical moments of the pressure field are calculated by averaging over a large number (some hundreds) of random, independent realizations.

The FDTD model predictions for the first- and second-order statistical moments are generally in very good

agreement with the analytical results—the latter being adapted to two-dimensional propagation. This supports the applicability of both in the selected scenarios. In the large scattering angle case, there is a discrepancy at very small scattering angles. It is caused by the finite size of the turbulent area, which alters the effective spectrum of the turbulent fluctuations—an effect which is ignored in the analytical approach. In the small scattering angle case, the terms neglected in the analytical approach under the high-frequency approximation are shown to explain the minor differences with the FDTD model predictions. The high-frequency approximation is a standard in parabolic equation (PE) approaches. Violation of it is argued to cause the inapplicability of the PE models and the line-of-sight analytical solution in the low frequency cases.

The present study shows that the FDTD solution of the two coupled equations is capable of simulating the impacts of turbulence effects at large and small scattering angles. This approach therefore overcomes the standard distinction with the scattering angle. These results also pave the way toward the assessment of less idealized atmospheric conditions. For example, the analytical results considered here are all obtained under a perturbation analysis. This approximation fails when the exciting wave is significantly altered from the free-field propagation. This may be the case if multiple scattering effects are non negligible in the scattering volume, e.g., as potentially caused by strong turbulence. The above modeling approach avoids this limitation and is a method of choice to assess the impact of strong perturbations. This topic is under current investigations (Ehrhardt *et al.*, 2011).

ACKNOWLEDGMENTS

This study was initiated in 2005 under the "Exploratory Research" framework of the ISL. The authors thank the two anonymous reviewers for their suggestions, and V. Ostashev (NOAA/ESRL and ERDC/CRREL) for his comments on an early version of the manuscript. The ISL Aerodynamics Department is acknowledged for providing access to their computational cluster.

Andreas, E. L. (**1987**). "Spectral measurements in a disturbed boundary layer over snow," J. Atmos. Sci. **44**, 1912–1939.

Aumond, P., Guillaume, G., Gauvreau, B., Picaut, J., Dutilleux, G., Lac, C., Masson, V., and Bérengier, M. (**2010**). "Couplage d'un modèle numérique météorologique avec le modèle numérique de propagation acoustique TLM" ("Coupling of a meteorological numerical model with a TLM numerical model for acoustic propagation"), *Actes du 10e Congrès Français d'Acoustique*, Lyon, France, available at http://hal-meteofrance.archives-ouvertes.fr/docs/00/54/26/06/PDF/000324.pdf (last viewed April 25, 2012), p. 4.

Brownlee, L. R., (**1974**). "Reply to 'Comments on 'Rytov's method and large fluctuations,'" J. Acoust. Soc. Am. **55**, 1339–1339.

Candel, S. M., (**1979**). "Numerical solution of wave scattering problems in the parabolic approximation," J. Fluid Mech. **90**, 465–507.

Cheinet, S. (**2012**). "A numerical approach to sound levels in near-surface refractive shadows," J. Acoust. Soc. Am. **131**, 1946–1958.

Cheinet, S., Beljaars, A., Weiss-Wrana, K., and Hurtaud, Y. (**2011**). "Weather forecasts to characterize the near-surface optical turbulence," Bound. Lay. Meterol. **138**, 453–473.

Cheinet, S., and Naz, P. (**2006**). "On-going ISL research in modelling acoustic propagation in the atmosphere," *NATO SET-107/RSY20/MSE Symposium*, Amsterdam, Netherlands, available at http://www.dtic.mil/cgi-bin/GetTRDoc?Location=U2&doc=GetTRDoc.pdf&AD=ADA478770 (last viewed 12 Oct. 2011), p. 11.

Chevret, P., Blanc-Benon, Ph., and Juvé, D. (**1996**). "A numerical model for sound propagation through a turbulent atmosphere near the ground," J. Acoust. Soc. Am. **100**, 3587–3599.

Clifford, S. F. (**1978**). "The classical theory of wave propagation in a turbulent medium," in *Laser Beam Propagation in the Atmosphere, Vol. 25 of Topics in Applied Physics* (Springer-Verlag, New York), pp. 9–43.

Clifford, S. F., and Brown, E. H. (**1970**). "Propagation of sound in a turbulent atmosphere," J. Acoust. Soc. Am. **48**, 1123–1127.

Colonius, T., Lele, S. K., and Moin, P. (**1994**). "The scattering of sound waves by a vortex: Numerical simulations and analytical solutions," J. Fluid Mech. **260**, 271–298.

Cotté, B., and Blanc-Benon, Ph. (**2007**). "Estimates of the relevant turbulent scales for acoustic propagation in an upward refracting atmosphere," Acta Acust. Acust. **93**, 1–15.

Coulter, R. L. (**1997**). "Turbulence variables derived from SODAR data," in Acoustic Remote Sensing Applications, Vol. 69 of Lecture Notes in Earth Sciences, edited by S. P. Singal (Narosa Publ. House, New Delhi), pp. 191–200.

Daigle, G. A. (**1979**). "Effects of atmospheric turbulence on the interference of sound waves above a finite impedance boundary," J. Acoust. Soc. Am. **65**, 215–248.

Daigle, G. A., Embleton, T. F. W., and Piercy, J. E. (**1986**). "Propagation of sound in the presence of gradients and turbulence," J. Acoust. Soc. Am. **79**, 613–627.

Dallois, L., and Blanc-Benon, Ph. (**2001**). "Wide angle parabolic equations in moving media: Sound diffraction by a core vortex," in *7th AIAA Conference on Aeroacoustics*, Report No. 2001-2256, pp. 856–864.

Dashen, R. (**1979**). "Path integrals for wave in random media," J. Math. Phys. **20**, 894–920.

Ehrhardt, L., and Cheinet, S. (**2010**). "Développement et évaluation d'un code de propagation acoustique en domaine temporal" ("Development and evaluation of a time-domain acoustic propagation model"), in *Actes du 10e Congrès Français d'Acoustique*, Lyon, France, available at http://cfa.sfa.asso.fr/cd1/data/articles/000560.pdf (last viewed 19 Oct. 2011), pp. 6.

Ehrhardt, L., Cheinet, S., and Juvé, D. (**2011**). "Scattering of plane waves by local inhomogeneities and turbulent fluctuations: comparison between theory and time-domain computations," in *Proceedings of the Fourteenth International Symposium on Long Range Sound Propagation*, Annapolis, available at http://ncpa.olemiss.edu/!documents/LRSP%20Presentations/LRSP%20Presentations%202011/LRSP/EL.pdf (last viewed 19 Oct. 2011).

Flatté, S. M., Dashen, R., Munk, W. H., Watson, K., and Zachariasen, F. (**1979**). *Sound Transmission through a Fluctuating Ocean* (Cambridge University Press, Cambridge), Chaps. 6–8.

Frehlich, R., Cornman, L., and Sharman, R. (**2001**). "Simulation of three-dimensional turbulent velocity fields," J. Appl. Meteorol. **40**, 246–258.

Gilbert, K. E., Raspet, R., and Di, X. (**1990**). "Calculation of turbulence effects in an upward-refracting atmosphere," J. Acoust. Soc. Am. **87**, 2428–2437.

Goedecke, G. H., and Auvermann, H. J. (**1997**). "Acoustic scattering by atmospheric turbules," J. Acoust. Soc. Am. **102**, pp. 759–771.

Havelock, D. I., Di, X., Daigle, G. A., and Stinson, M. R. (**1995**). "Spatial coherence of a sound field in a refractive shadow: Comparison of simulation and experiment," J. Acoust. Soc. Am. **98**, 2289–2302.

Hinze, J. O. (**1959**). *Turbulence* (McGraw-Hill, New York), Chap. 3.

Jensen, F. B., Kupermann, W. A., Porter, M. B., and Schmidt, H. (**2000**). *Computational Ocean Acoustics* (Springer, New York), Chap. 6.

Kallistratova, M. A. (**1997**). "Physical grounds for acoustic remote sensing of the atmospheric boundary layer," in *Acoustic Remote Sensing Applications, Vol. 69 of Lecture Notes in Earth Sciences*, edited by S. P. Singal (Narosa Publ. House, New Delhi), pp. 3–34.

Kallistratova, M. A. (**2002**). "Acoustic waves in a turbulent atmosphere: A review," J. Atmos. Ocean. Technol. **19**, 1139–1150.

Kaimal, J. C. (**1973**). "Turbulence spectra, length scales and structure parameters in the stable surface layer," Bound. Layer Meteorol. **4**, 289–309.

Kaimal, J. C. (**1978**). "Horizontal velocity spectra in an unstable surface layer," J. Atmos. Sci. **35**, 18–24.

Lawrence, R. S., and Strohbehn, J. W. (**1970**). "A survey of clear-air propagation effects relevant to optical communications," Proc. IEEE **58**, 1523–1545.

Martin, J. M., and Flatté, S. M. (**1988**). "Intensity images and statistics from numerical simulation of wave propagation in 3-D random media," Appl. Opt. **27**, 2111–2126.

McBride, W. E., Bass, H. E., Raspet, R., and Gilbert, K. E. (**1991**). "Scattering of sound by atmospheric turbulence: A numerical simulation above a complex impedance boundary," J. Acoust. Soc. Am. **90**, 3314–3325.
McLeod, I. D., C. G. Don and G. G. Swenson, (**2004**). "Acoustic pulse propagation in an outdoor turbulent atmosphere," J. Acoust. Soc. Am. **116**, 2855–2863.
Ostashev, V. E. (**1994**). "Sound propagation and scattering in media with random inhomogeneities of sound speed, density and medium velocity," Waves Rand. Med. **4**, 403–418.
Ostashev, V. E. (**1997**). *Acoustics in Moving Inhomogeneous Media* (E&F Spon, London), Chaps. 2, 6, and 7.
Ostashev, V. E., Blanc-Benon, Ph., and Juvé, D. (**1997**). "Derivation of a wide-angle parabolic equation for sound waves in inhomogeneous moving media," Acta Acust. Acust. **83**, 455–460.
Ostashev, V. E., Salomons, E. M., Clifford, S. F., Lataitis, R. J., Wilson, D. K., Blanc-Benon, Ph., and Juvé, D. (**2001**). "Sound propagation in a turbulent atmosphere near the ground: A parabolic equation approach," J. Acoust. Soc. Am. **109**, 1894–1908.
Ostashev, V. E., and Wilson, D. K. (**2001**). "Log-amplitude and phase fluctuations of a plane wave propagating through anisotropic, inhomogeneous turbulence," Acta Acust. Acust. **87**, 685–694.
Ostashev, V. E., Wilson, D. K., Liu, L., Aldridge, D. F., Symons, N. P., and Marlin, D. (**2005**). "Equations for finite-difference, time-domain simulation of sound propagation in moving inhomogeneous media and numerical implementation," J. Acoust. Soc. Am. **117**, 503–517.
Panofsky, H. A. (**1969**). "The spectrum of temperature," Radio Sci. **4**, 1143–1146.
Salomons, E. M. (**2000**). "Fluctuations of spherical waves in a turbulent atmosphere: Effect of the axisymmetric approximation in computational methods," J. Acoust. Soc. Am. **108**, 1528–1534.
Strohbehn, J. W. (**1968**). "Line-of-sight wave propagation through the turbulent atmosphere," Proc. IEEE **56**, 1301–1318.
Symons, N. P., Aldridge, D. F., Marlin, D. H., Wilson, D. K., Patton, E. G., Sullivan, P. P., Collier, S. L., Ostashev, V. E., and Drob, D. P. (**2004**). "3D staggered-grid finite-difference simulation of sound refraction and scattering in moving media," in *Proceedings of the 11th International Symposium on Long Range Sound Propagation*, Fairlee, VT, available at http://ncpa.olemiss.edu/long-range-sound-propagation-lrsp/ (last viewed 23 April 2012), p. 19.
Tatarski, V. I. (**1961**). *Wave Propagation in a Turbulent Medium* (McGraw-Hill, New York), p. 285.
Tatarski, V. I. (**1971**). *The Effects of the Turbulent Atmosphere on Wave Propagation*, translated from the Russian by the Israel Program for Scientific Translations, Jerusalem, 1971, available from the U.S. Department of Commerce, National Technical Information Service, Springfield, VA, p. 471.
Vecherin, S. N., Ostashev, V. E., Goedecke, G. H., Wilson, D. K., and Voronovich, A. G. (**2006**). "Time-dependent stochastic inversion in acoustic travel-time tomography of the atmosphere," J. Acoust. Soc. Am. **119**, 2579–2588.
Wheelon, A. D. (**2003**). *Electromagnetic Scintillation: 2. Weak Scattering* (Cambridge University Press, Cambridge), p. 460.
Wiener, F. M., and Keast, D. N. (**1959**). "Experimental study of the propagation of sound over ground," J. Acoust. Soc. Am. **31**, 724–733.
Wilson, D. K., and Liu, L. (**2004**). "Finite-difference, time-domain simulation of sound propagation in a dynamic atmosphere," ERDC/CREEL Technical Report No. TR-04-12, p. 56.
Wilson, D. K., and Thomson, D. W. (**1994**). "Acoustic tomographic monitoring of the atmospheric surface layer," J. Atmos. Ocean. Tech. **11**, 751–769.
Wilson, D. K., Wyngaard, J. C., and Havelock, D. I. (**1996**). "The effect of turbulence intermittency on the scattering into an acoustic shadow zone," J. Acoust. Soc. Am. **99**, 3393–3400.
Ye, Zh. (**1997**). "Sound scattering from a moving turbulent medium," J. Acoust. Soc. Am. **102**, 752–758.
Yura, H. T., Sung, C. C., Clifford, S. F., and Hill, R. J. (**1983**). "Second-order Rytov approximation," J. Opt. Soc. Am. **73**, 500–502.